FISEVIER

Contents lists available at ScienceDirect

Materials Science & Engineering A

journal homepage: www.elsevier.com/locate/msea



Hydrogen-induced compatibility constraints across grain boundaries drive intergranular failure of Ni



K.M. Bertsch^{a,b,c,*}, S. Wang^{d,e}, A. Nagao^{b,f}, I.M. Robertson^{c,d,**}

- ^a Department of Materials Science and Engineering, University of Illinois at Urbana-Champaign, Urbana, IL, 61801, USA
- b International Institute for Carbon-Neutral Energy Research (WPI-12CNER), Kyushu University, 744 Motooka, Nishi-ku, Fukuoka, 819-0395, Japan
- ^c Department of Materials Science and Engineering, University of Wisconsin-Madison, Madison, WI, 53706, USA
- d Department of Engineering Physics, University of Wisconsin-Madison, Madison, WI, 53706, USA
- e Department of Mechanical and Energy Engineering, Southern University of Science and Technology, 1088 Xueyuan Blvd, Shenzhen, 518055, China
- Material Surface & Interface Science Research Department, Steel Research Laboratory, JFE Steel Corporation, 1-1 Minamiwatarida-cho, Kawasaki-ku, Kawasaki, Kanagawa, 210-0855, Japan

ARTICLE INFO

Keywords: Hydrogen embrittlement Multi-scale Grain boundaries Hydrogen-enhanced plasticity

ABSTRACT

A multi-scale experimental approach was used to determine the fundamental mechanisms responsible for the hydrogen-induced transition in failure mode from ductile transgranular to intergranular in polycrystalline Ni during uniaxial loading. Hydrogen accelerated the evolution of the deformation microstructure, producing smaller dislocation cells and microbands, and causing significantly different orientation deviations to develop in neighboring grains, while inducing less evolution of texture, less grain rotations, less elongation of the grains parallel to the tensile axis, and greater out-of-surface distortion of the grains. These observations are explained in terms of the hydrogen-enhanced plasticity mechanism, which results in a redistribution of hydrogen that stabilizes the deformed microstructure and increases the hydrogen coverage on the grain boundaries. The stabilization of the microstructure manifests as a reduced ability of grains to cooperatively accommodate evolving deformation structures, which introduces an additional compatibility constraint across grain boundaries. The combination of this compatibility constraint across grain boundaries, the locking of the microstructure in a specific configuration by hydrogen, and the hydrogen-weakening of the grain boundaries drives the hydrogen-induced intergranular failure.

1. Introduction

During plastic deformation of a polycrystalline metal, the slip systems activated within a grain are determined by the orientation of the grain with respect to the loading axis, such that grain orientation determines the evolution of dislocation structures [1], the rotation of the grains [2,3], and, thus, the texture evolution. Although these dependencies are well-established for FCC metals and alloys, the role, if any, of hydrogen on the evolution of dislocation structures, grain morphology, and texture as a function of strain has received little attention. This is somewhat surprising as these changes determine the overall mechanical response and the failure mode. This manuscript provides insight as to how hydrogen influences the deformation response with a particular application to hydrogen-induced intergranular fracture.

In hydrogen-induced intergranular failure [4–23], which occurs by decohesion along the grain boundary, there is debate about the need for an additional driving force to cause the failure [18,20–22,24]. Evidence supporting the need for additional forces are that the stress-strain response is in some metals similar in the absence and presence of hydrogen until the onset of the necking instability [22,24]; the evidence of general plasticity including on intergranular facets [18,20,23]; and computational studies that question if a sufficient hydrogen concentration can be achieved on a grain boundary under practical charging conditions [20,25–29]. For example, the mechanical properties of an uncharged and hydrogen-charged equi-molar FeNiCoCr alloy were: yield strengths, 170 and 192 MPa; ultimate tensile strengths, 562 and 560 MPa, and strains to failure, 68.1% and 63.5% in the uncharged and hydrogen-charged materials, respectively. However, the failure mode changed from ductile microvoid coalescence to predominantly

^{*} Corresponding author.

^{**} Corresponding author. Department of Materials Science and Engineering, University of Wisconsin-Madison, Madison, WI, 53706, USA. *E-mail addresses*: kbertsch@wisc.edu (K.M. Bertsch), wangs@sustc.edu.cn (S. Wang), akihidenagao@gmail.com (A. Nagao), irobertson@wisc.edu (I.M. Robertson).

intergranular in the hydrogen-charged alloy [22]. Recent studies of the dislocation structures beneath fracture surfaces suggest hydrogen accelerates the evolution of the dislocation microstructures, causes more out-of-plane displacement, reduces the extension of grains in the tensile direction, and, in some metals and alloys, causes a change in fracture mode from transgranular to intergranular [18,19,21,22,30]. Based on these observations, it was proposed that the additional driving force generated by hydrogen-accelerated plasticity processes established the local conditions for intergranular failure. That is, as the local microstructural stresses in addition to the increasing applied load could no longer be supported by dislocation slip, fracture occurred along the weakest links in the system, which were the hydrogen-weakened grain boundaries. This mechanism is in marked contrast to the classic decohesion explanation in which hydrogen decreases the cohesive strength sufficiently to cause failure and any plasticity is irrelevant to the failure [7-9,11-14,17,23,24].

In this study, the evolution of the microstructure during uniaxial tensile deformation was compared in uncharged and hydrogen-charged commercially pure Ni. A comprehensive understanding of the influence of hydrogen on the evolution of the microstructure and its correlation with the failure path was obtained by using characterization tools that spanned a range of spatial scales. This enabled assessment of the influence of hydrogen on the rotation of individual grains, on the grain morphology, on the local rotations within a grain, and on the evolution of the deformation microstructure in the absence and presence of hydrogen. Considered separately some of the results could be interpreted as hydrogen causing a reduction of the plasticity and others as hydrogen increasing the plasticity. However, when considered collectively and within the framework of the hydrogen-enhanced plasticity mechanism, a self-consistent explanation of all effects can be achieved. Effectively, hydrogen effects on the plasticity and in locking the microstructure in a specific configuration results in a difference in the magnitude of deformation across a grain boundary. That is, communication of strain across the grain boundary is impeded. In addition, hydrogen transport by dislocations to and from the grain boundary increases the hydrogen concentration on the grain boundary. This additional constraint across the grain boundary, the locked microstructure, and the increased hydrogen concentration on the grain boundary ultimately lead to failure along the hydrogen-weakened grain boundary.

2. Experimental procedure

Flat, hourglass-shaped tensile specimens were cut from Ni sheet (purity > 99.76%) of thickness 1 mm using electrical discharge machining. Specimen grip ends were 12 mm long, the total length of the center reduced section was 24 mm, and the width was smoothly graded along the reduced section such that it was 3 mm wide at the center and 10 mm wide at the grip ends, yielding a radius of curvature of 22.3 mm. All specimens were annealed at 700 °C for 8 h prior to some samples being hydrogen charged. Hydrogen charging was performed in an autoclave in a 120 MPa gaseous $\rm H_2$ environment at 200 °C for 160 h. Thermal desorption analysis was used to analyze the hydrogen content in the hydrogen-charged specimens; the ramp rate for this analysis was 200 °C h $^{-1}$ from room temperature to 800 °C.

Tensile tests were performed at room temperature with a constant displacement rate of $2\times 10^{-4}\,\mathrm{mm\,s^{-1}}$. An uncharged specimen was tested to failure in an Instron E10000 ElectroPuls load frame at the University of Wisconsin-Madison. A hydrogen-charged specimen was strained to failure in situ in an FEI NOVA nanoSEM equipped with a hydraulic load cell at Purdue University. Further, uncharged and hydrogen-charged specimens were tested to specific strains using an MTS QTest/5 tensile machine with a 5 kN load cell at the University of Wisconsin-Madison; these tests were interrupted at prescribed, equivalent macroscopic strains.

The structures and morphology along the reduced section of each

specimen and on the fracture surfaces were investigated using a Zeiss LEO 1530 Gemini field emission scanning electron microscope (SEM) operated at 20 kV. Electron backscattered diffraction (EBSD) analysis of the grains along the reduced section was performed in a Zeiss LEO 1530 Gemini SEM operated at 20 kV or in an FEI Helios G4 plasma focused ion beam (PFIB) CXe with an Elstar SEM column. EBSD measurements in the PFIB were acquired using an Hikari EBSD camera and an accelerating voltage of 20–30 kV. EBSD mapping was conducted using step sizes between 0.75 and 2 μm , and maps consisted of areas 0.5–1 mm wide by 1.5–2.5 mm long.

Thin foils were extracted from the specimen surfaces along the reduced section and from the fracture surfaces for scanning/transmission electron microscopy (S/TEM) analysis using a Zeiss Auriga model Ga FIB with the ion accelerating voltage varied between 5 and 30 kV. A protective Pt layer was deposited prior to ion milling to preserve surface features. The final polish of electron transparent foils was performed using a 5 kV Ga ion beam. S/TEM analysis was performed in an FEI Tecnai TF-30 S/TEM operated at 300 kV. Orientation maps of the electron transparent foils were produced utilizing the ASTAR automated crystal orientation mapping system [31] with an angular resolution of 0.1–0.2° attached to the TF-30, typically using a step size of 12.5–17.5 nm. Analysis of all orientation mapping data was performed using the MTEX software package for MATLAB [32] and custom MATLAB functions.

3. Results

The initial microstructure was a random distribution of equiaxed grains with an average grain size between 50 and 100 µm. The hydrogen-charging resulted in an internal hydrogen concentration of 27.4 mass ppm (1606 atomic ppm). The uncharged specimen failed through transgranular ductile microvoid coalescence at approximately 26% strain, and the hydrogen-charged specimen failed at approximately 15% strain by intergranular fracture. The out-of-surface distortions along the gauge length were qualitatively larger and extended further along the gauge length in hydrogen-charged than in uncharged Ni. Secondary microcracking along grain boundaries was found on the fracture surface and along the reduced section at strains of at least 9.5% in hydrogen-charged specimens. On the intergranular facets on the fracture surface, there was evidence of slip steps. These features of the embrittlement are captured in Fig. 1, which shows the engineering stress-strain data, Fig. 1a (--- uncharged and ___ hydrogen-charged), SEM images of the specimen surface showing the out-of-surface distortion Fig. 1b uncharged and Fig. 1c hydrogen-charged, and fractographs of the ductile knife-edge failure in uncharged Ni in which the arrowheads mark the knife-edge, Fig. 1d, and the intergranular facets in hydrogen-charged Ni, Fig. le. The stress-strain response and the change in failure mode are consistent with the results presented in other studies of hydrogen embrittlement in Ni [6,10,12,15,18,24,33].

EBSD analysis of the undeformed and deformed uncharged and hydrogen-charged Ni revealed that only in uncharged Ni did the texture evolve towards < 111 > parallel to the tensile axis. This difference is highlighted for specimens strained to failure in the inverse pole figures shown in Fig. 2; the regions selected for analysis in the deformed samples were approximately 3 mm from the fracture surfaces and 500 points were randomly selected from EBSD data. Prior to straining, the undeformed uncharged, Fig. 2a, and hydrogen-charged, Fig. 2c, Ni exhibited similar random orientation distributions. Following deformation, there was an accumulation of points near [111] in uncharged Ni, Fig. 2b, which is consistent with the anticipated rotations and corresponding texture evolution. In the hydrogen-charged sample, points were distributed throughout the stereographic triangle, with some minor accumulation of points near [001]. These differences in the texture evolution could be attributed to the difference in the failure strain or reflect hydrogen limiting texture evolution. The latter explanation could be taken as evidence of hydrogen reducing the

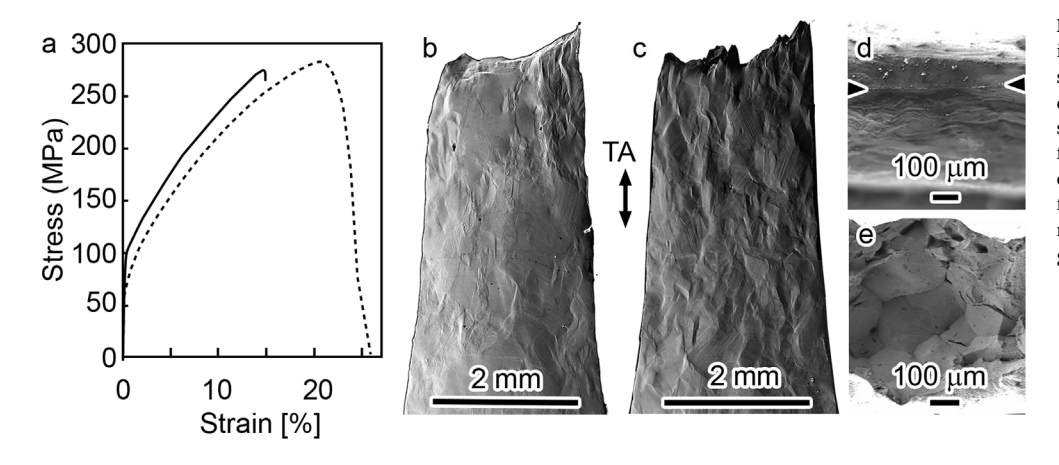


Fig. 1. Effects of hydrogen on the mechanical properties of Ni. a. engineering stress-strain curves (—— uncharged and ___ hydrogen-charged); b and c SEM images of the specimen surface showing the out-of-surface distortions in uncharged and hydrogen-charged Ni, respectively; d knife-edge failure in uncharged Ni in which the arrowheads mark the knife-edge; and e intergranular facets in hydrogen-charged Ni.

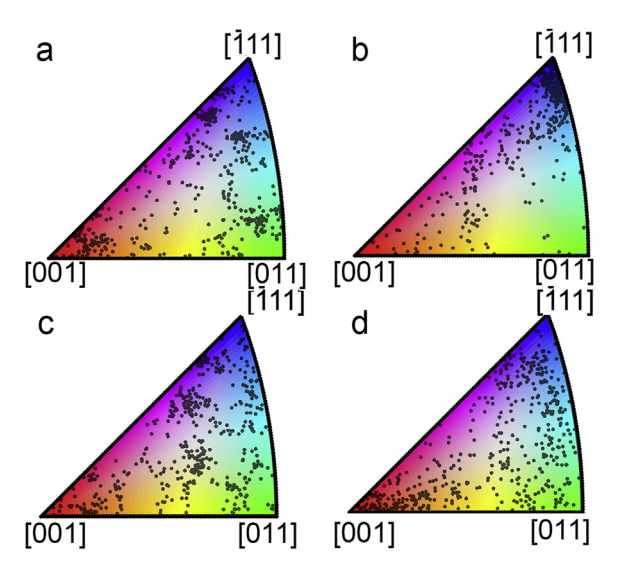


Fig. 2. The evolution of texture in: a. undeformed and b. deformed uncharged Ni; c. undeformed and d. deformed hydrogen-charged Ni. Specimens b and d were strained to failure at 26% strain and 15% strain, respectively. Color online. (For interpretation of the references to color in this figure legend, the reader is referred to the Web version of this article.)

plasticity.

The shape of grains changed with deformation, with the elongation parallel to the tensile axis and the increase in area being greatest in the uncharged material. These changes can be seen by comparing the EBSD maps of the same area before and after 9.5% strain; Fig. 3a and b shows the change in uncharged Ni, and Fig. 3c and d in hydrogen-charged Ni.

To make the differences between uncharged and hydrogen-charged Ni clearer, the outlines of a few grains before (black boundaries) and after (blue boundaries) deformation to 9.5% strain are superimposed for uncharged and hydrogen-charged Ni in Fig. 3e and f, respectively; the overlay was made by aligning the centroids of the grains. The change in shape is evident and it is greatest in uncharged Ni. This result when considered in isolation could be interpreted as hydrogen reducing the plasticity.

To evaluate the evolution of orientation of individual grains, the rotation of select individual grains was assessed at different strains in both uncharged and hydrogen-charged specimens. The average orientation of each selected grain was determined prior to and after deformation by EBSD analysis of the same areas, see Fig. 3, and the angle of rotation was calculated from Euler angles. A comparison of the response of select grains at 9.5% strain in uncharged and hydrogencharged Ni is shown in Fig. 4; the average orientation of the grain in the loading direction after straining is indicated by the dot and is connected to the initial average orientation by a line. As only the initial and final average orientations were determined, the lines do not necessarily indicate the evolution pathway. From Fig. 4, it can be seen that grains with an initial orientation near [111] rotated towards [111], grains with an initial orientation near [001] rotated in random directions but remained close to [001], and those initially near [011] rotated mainly towards the line between [001] and [111] or towards [111], both in the absence and presence of hydrogen. Qualitatively, the data presented in Fig. 4 suggests the response of individual grains follows the same trends in uncharged and hydrogen-charged Ni. However, differences emerged when the average magnitude of rotation was considered, see Fig. 4c. In this figure, the square symbols correspond to 8.0% strain and circles to 9.5% strain; open symbols represent uncharged, and filled symbols hydrogen-charged Ni. The response in uncharged Ni for strains of 8.0%

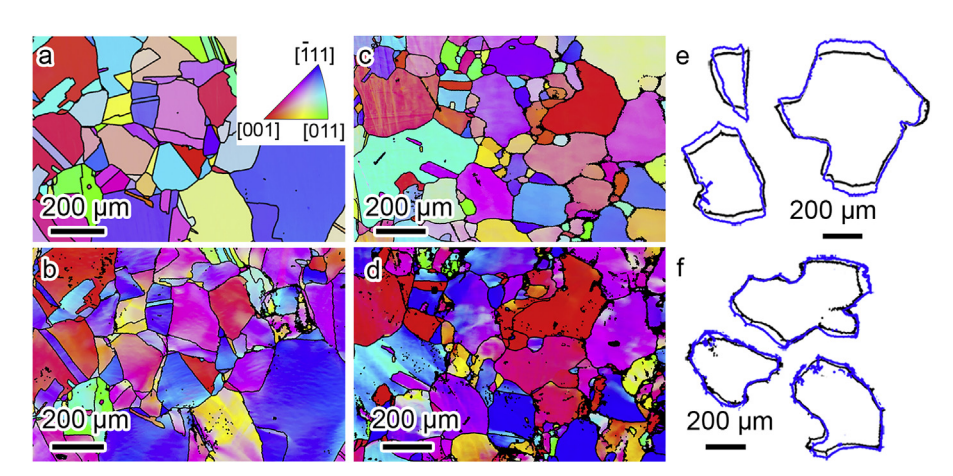


Fig. 3. EBSD maps comparing the change in the shape of grains following deformation to 9.5% strain. a and b. undeformed and deformed uncharged Ni, respectively; c and d. undeformed and deformed hydrogencharged Ni; e overlaid undeformed and deformed grains in uncharged Ni; and f. overlaid undeformed and deformed grains in hydrogen-charged Ni. Initial grain boundary shape in black and final shape after deformation in blue. Tensile axis is vertical. Color online. (For interpretation of the references to color in this figure legend, the reader is referred to the Web version of this article.)

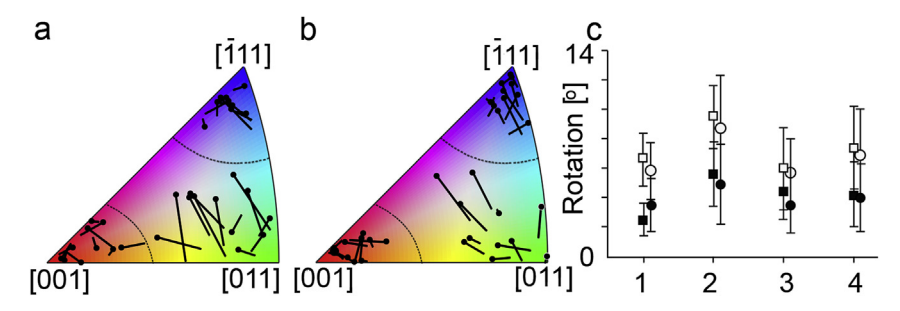


Fig. 4. Rotation of grains from initial to final position following 9.5% strain of: a. uncharged and b. hydrogencharged Ni. The lines represent the direction and magnitude of the rotation, with the final orientation indicated by the dot. c. Average magnitude of rotation of selected grains with strain, grouped by initial grain orientations of 1near <001>, 2 near <011>, 3 near <111> and 4. average. Open symbols, uncharged Ni, and filled symbols, hydrogencharged Ni. Squares 8.0% strain and circles 9.5% strain. Color online. (For interpretation of the references to color in this figure legend, the reader is referred to the Web version of this article.)

and 9.5% was as expected, with the average angular rotation being largest for grains with an initial orientation near [011], followed by near [001] grains, and finally grains near[111]. For hydrogen-charged Ni, the same trends with respect to the initial grain orientation were observed except for near [001] grains at 8.0% strain, which showed the smallest of all rotations. However, irrespective of the initial grain orientation, the average magnitude of the rotation was always smaller in hydrogen-charged than in uncharged Ni by approximately 42%. The results presented in Fig. 4c show that the grain rotations are smaller in the presence of hydrogen for the same macroscopic strains, which is consistent with the texture being less evolved in hydrogen-charged than in uncharged Ni. That is, the preferred orientation results presented in Fig. 2 for failed specimens are not entirely attributable to the difference in the magnitude of the failure strain. From Fig. 4c, it is noted that the average rotation of grains in specimens following 8.0% strain was slightly higher than that measured for specimens following 9.5% strain, although the difference is within the measurement error. Any significant difference likely reflects the randomness of the position of the selected grains, variations in deformation pathway and the influence of neighboring grains on the deformation. This result when considered in isolation could be interpreted as hydrogen reducing the plasticity.

In addition to exploring the overall rotation of individual grains, the orientation deviation of each sampled point inside a grain from the calculated mean grain orientation was determined from EBSD data. The results showed qualitatively that non-uniform orientation deviations across the grain interior were most prevalent in hydrogen-charged Ni. In uncharged Ni, the largest orientation deviations tended to cluster around grain boundaries, typically leaving a relatively contiguous region of low orientation deviation from the mean grain orientation near the grain center. Conversely, regions with large orientation deviations extended across the entire grain in discontinuous segments in hydrogen-charged Ni. Examples of these differences at 9.5% strain can be seen in the images presented in Fig. 5a and b for the uncharged and hydrogen-charged Ni, respectively. This difference in orientation deviation within individual grains with respect to the mean is quantified at two locations for both uncharged (red distribution) and hydrogencharged (blue) Ni after straining to 9.5% in the histograms (bin size, 0.25°) presented in Fig. 5; Fig. 5c is from the center of the gauge section and Fig. 5d is from a region 3 mm from the center. In the undeformed material, the distribution (not shown) was clustered between 0 and 2°, indicating a well-annealed initial microstructure. The distribution peaks at both locations and in the charged and hydrogen-charged Ni are similar, although higher angle deviations occurred most frequently in hydrogen-charged Ni. This latter result suggests that the plastic deformation is locally higher in the hydrogen-charged alloy.

The orientation deviation distributions after failure were compared both near the fracture surfaces and 3 mm from them, see Supplemental Fig. 1. At the fracture surface, the peak of the distribution shifted to a higher angle in the uncharged Ni, showing the impact of the severe necking that occurred. Away from the fracture surface, the peak in the distribution in the hydrogen-charged case shifted to a larger value than in the uncharged case, despite the lower failure strain. This result is consistent with hydrogen influencing the plasticity along the gauge

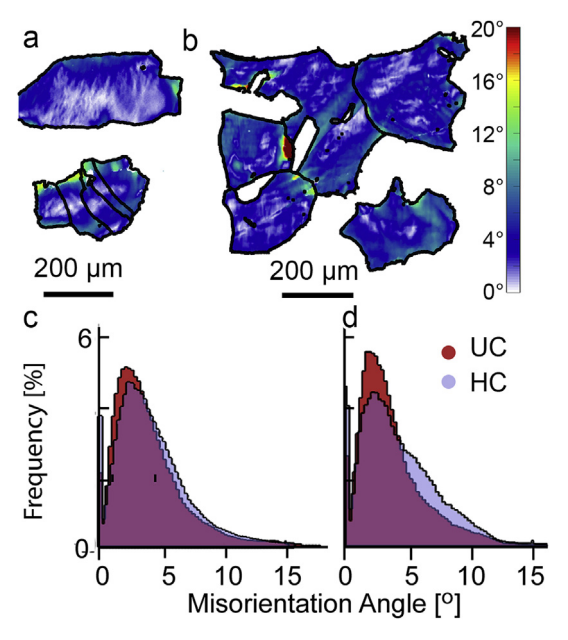


Fig. 5. Orientation deviation maps with respect to the mean orientation of select grains in: a. uncharged and b. hydrogen-charged Ni following 9.5% strain. Distribution histograms of orientation deviations with respect to the mean orientation in multiple grains in uncharged and hydrogen charged Ni following 9.5% strain: c. center of reduced section and d. 3.0 mm from it; Reduncharged, blue-hydrogen-charged Ni, lavender – overlapping distributions. Color online. (For interpretation of the references to color in this figure legend, the reader is referred to the Web version of this article.)

length, which is important to understand the formation of microcracks along the gauge length.

To interpret the findings described in Figs. 1-5 in terms of dislocation structures, the microstructure was examined as a function of strain, position along the reduced gauge section, grain orientation, and proximity to a grain boundary. Multiple grain boundaries were examined and these were predominantly high-angle grain boundaries although some low-angle grain boundaries were included in the analysis. In addition to extracting samples from along the gauge section, samples were extracted from mating intergranular facets. In general, irrespective of the sample location, the microstructure in uncharged and hydrogen-charged Ni consisted of a dislocation cell structure with dislocation bands. However, there were notable differences. In the presence of hydrogen, the dislocation cell structure was more organized, the cell size was smaller and cell walls thicker, and the density of dislocation bands was higher. Further, there were notable differences in the misorientations that developed in neighboring grains in hydrogencharged specimens compared to those in uncharged specimens. Overall, the resultant differences in the microstructure were independent of the type of grain boundary and the initial grain orientation. Examples illustrating the differences attributable to the presence of hydrogen are shown in Figs. 6 - 11.

Irrespective of the initial orientation of the grain, the presence of

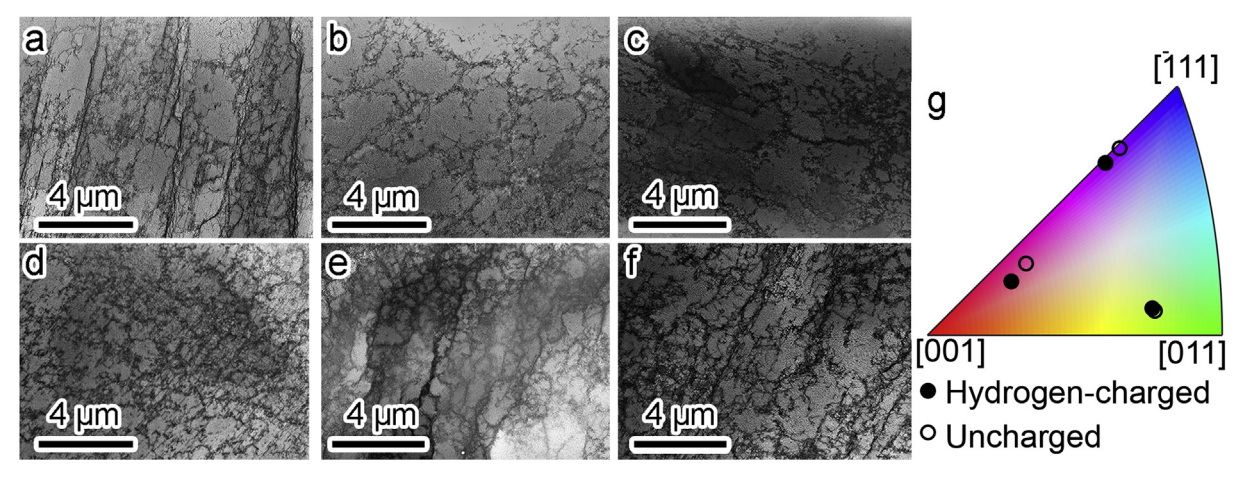


Fig. 6. Microstructures at 8.0% strain for grains oriented near a. [011], b. [001], and c. [11]. In uncharged Ni, and for grains oriented near d. [011], e. [001], and f. [111]. In hydrogen-charged Ni. g. Orientations prior to deformation in the loading direction of grains from which TEM specimens were extracted for uncharged (open circles) and hydrogen-charged (filled circles) samples. Color online. (For interpretation of the references to color in this figure legend, the reader is referred to the Web version of this article.)

hydrogen accelerated the development of the deformation microstructure. The differences at strains of 8.0% and 9.5% in the uncharged and hydrogen-charged materials are compared in the micrographs presented in Figs. 6 and 7, respectively. For the specimens deformed to 8.0% strain, the dislocation structures for grains with initial orientations near [011], near [001], and near [111] are shown in Fig. 6a, b, and 6c, respectively, for uncharged Ni; and in Fig. 6d, e, and 6f, respectively, for hydrogen-charged Ni. The orientations of the grains from which the samples were extracted prior to loading for the uncharged and hydrogen-charged samples are indicated by open and filled circles in Fig. 6g, respectively. The organization of the electron micrographs in Fig. 7 is identical to that in Fig. 6, but the samples were strained to 9.5%. In uncharged Ni, at both 8.0% and 9.5% strain, the formation of a dislocation cell structure was sporadic, with some regions containing dislocation tangles and others the initial stages of cell formation. Some organization of dislocations into walls along crystallographic planes is evident in Figs. 6a and 7c, but the misorientation across the walls was not sufficient to assert that geometrically necessary boundaries, GNBs, had formed. The dislocation structures observed in Fig. 6a-c and 7a-7c indicate that the organization of the deformation structure was still in the nascent phase.

In hydrogen-charged Ni, the dislocation structure was qualitatively further developed than in uncharged Ni; compare Fig. 6d-f with 6a-6c;

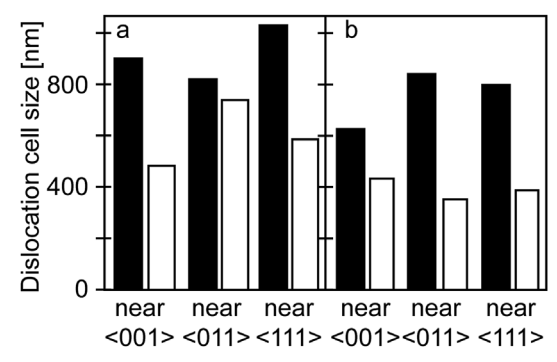


Fig. 8. Average dislocation cell diameters for grains oriented near the specified orientations in: a. specimens strained to 8% and b. specimens strained to 9.5%. Uncharged filled bars, hydrogen-charged open.

and Fig. 7d-f with 7a - 7c. Irrespective of the initial grain orientation and the magnitude of the strain, a dislocation cell structure extended over most of the grain interior and double-walled microbands existed in multiple grains at 9.5% strain in hydrogen-charged Ni; examples are indicated by arrowheads in Fig. 7d and e. The microbands appeared to shear the dislocation cell structures, causing steps in the otherwise

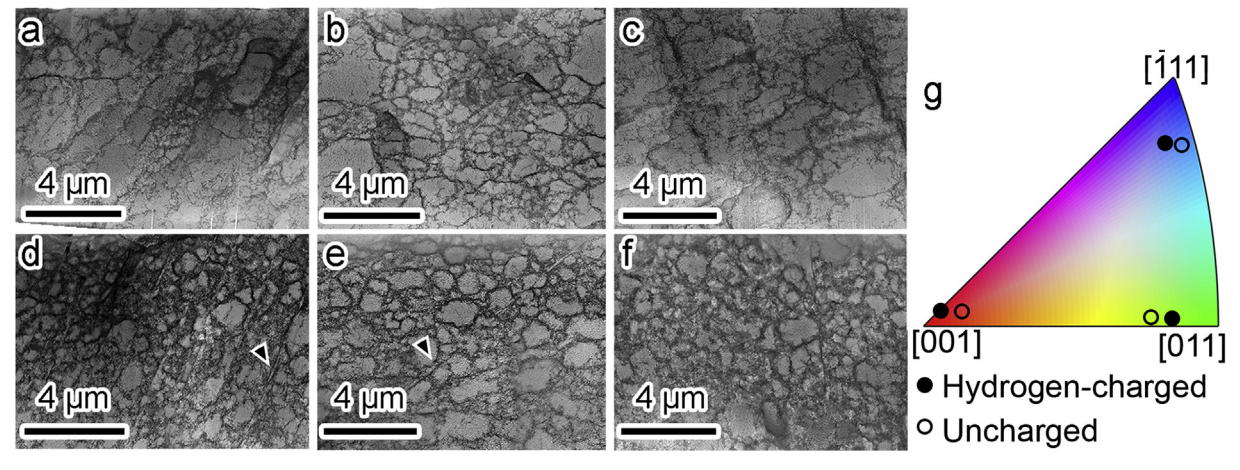


Fig. 7. Microstructures at 9.5% strain for grains oriented near: a. [011], b. [001], and c. [$\bar{1}$ 11]. In uncharged Ni, and for grains oriented near d. [011], e. [001], and f. [$\bar{1}$ 11]. In hydrogen-charged Ni. g. Orientations prior to deformation in the loading direction of grains from which TEM specimens were extracted for uncharged (open circles) and hydrogen-charged (filled circles) samples. Color online. (For interpretation of the references to color in this figure legend, the reader is referred to the Web version of this article.)

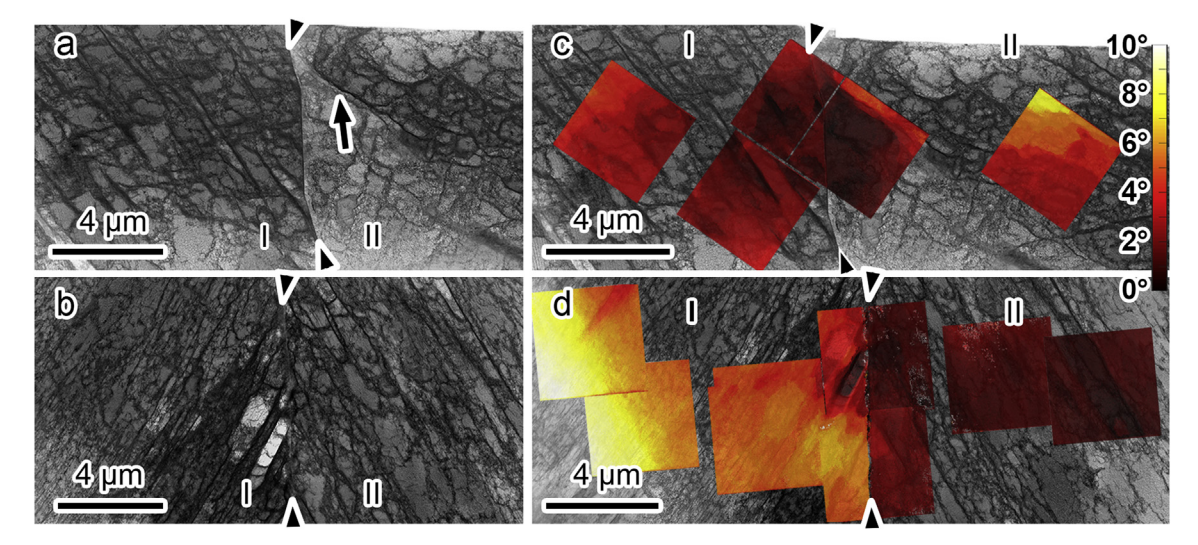


Fig. 9. Dislocation structures across a grain boundary 2 mm away from the fracture surface in: a. uncharged and b. hydrogen-charged Ni. Grain boundaries indicated by arrowheads. Reference orientation deviation maps overlaid on microstructures in: c. uncharged and d. hydrogen-charged Ni. Color online. (For interpretation of the references to color in this figure legend, the reader is referred to the Web version of this article.)

nearly-equiaxed cells, which implies the microbands formed after the cells. Misorientation measurements across microband walls indicate that they may be classified as "second-generation" microbands [34]. That is, in the presence of hydrogen the dislocation structure was further developed than in the absence of hydrogen, which is consistent with hydrogen enhancing the plasticity.

To quantify these differences, the dislocation cell size was measured as a function of initial grain orientation at 8.0% and 9.5% strain. The results, presented in Fig. 8, confirm that the average size of approximately equiaxed cells was larger in uncharged than in hydrogencharged Ni irrespective of the initial grain orientation. Additionally, the dimensions of the dislocation cell structure were measured as a function of distance from the fracture surfaces. This analysis showed that despite the difference in the failure strains, the dislocation cell sizes were of similar dimensions as a function of distance from the fracture surface; this data is provided as Supplemental Fig. 2. These results suggest that the presence of hydrogen was accelerating the evolution of the microstructure relative to the level of macroscopic strain and this influence extended along the entire gauge length. This finding has implications for the formation of the microcracks on the grain boundaries along the gauge length in hydrogen-charged Ni.

As the failure path is changed to be along the grain boundary by the presence of hydrogen, identifying differences in the evolved microstructural state near grain boundaries in uncharged and hydrogen-charged Ni is essential. Overall, the evolved microstructural state was independent of the type of grain boundary or the initial grain orientation but there were notable differences in uncharged and hydrogen-charged Ni. Examples of the deformation structures in the vicinity of grain boundaries are presented in Figs. 9-11.

The first example, presented in Fig. 9, shows the differences in the microstructure and the development of the misorientation differences at an intact grain boundary in uncharged and hydrogen-charged Ni. These samples were extracted approximately 2 mm along the gauge length from the fracture surfaces. In uncharged Ni, the dislocation structures in the adjacent grains (labeled I and II) across a $54.6^{\circ}9\,11$ grain boundary are shown in Fig. 9a; the grain boundary is indicated by arrowheads. Dislocation structures in the grain interiors consisted of either an equiaxed dislocation cell structure or dislocation cells accompanied by extended, high-angle dislocation walls. These dislocation walls were frequently distorted, particularly near grain boundaries and where they intersected other dislocation walls. An example of a distorted band is indicated by the arrow in Fig. 9a. The grain boundaries

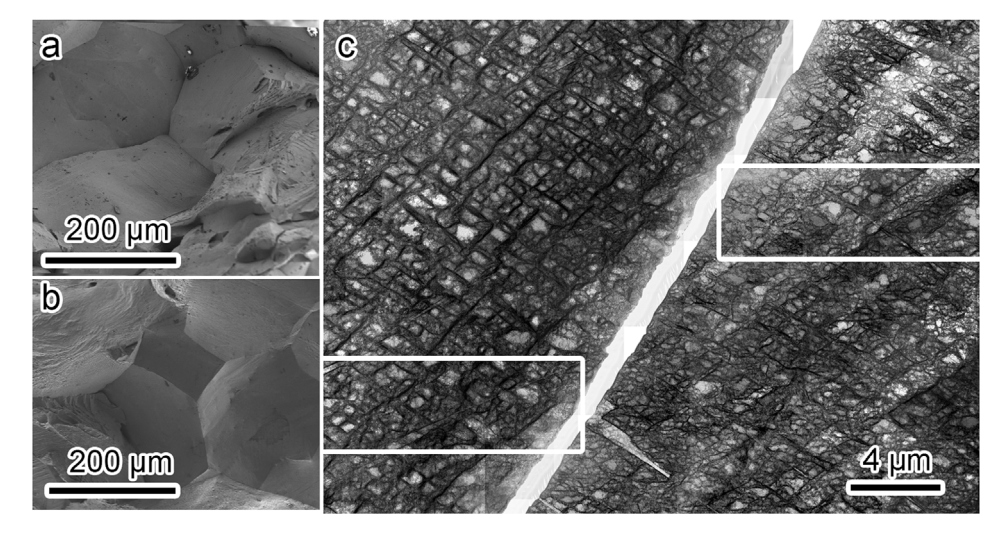


Fig. 10. Dislocation structures beneath the intergranular facets on opposite sides of the fracture surface in hydrogen-charged Ni: a. and b. fractographs, c. bright-field STEM images of microstructures beneath opposite sides of the fracture surface. ROD maps of boxed regions shown in Fig. 11.

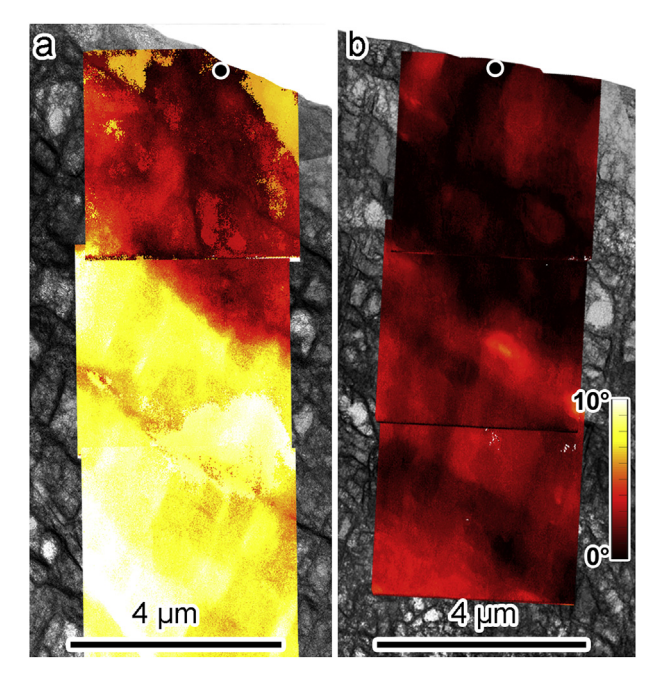


Fig. 11. Reference orientation deviation maps beneath the intergranular facets on opposite sides of the fracture surface in hydrogen-charged Ni. Regions selected shown in Fig. 10. Color online. (For interpretation of the references to color in this figure legend, the reader is referred to the Web version of this article.)

were curved and frequently contained steps that were approximately 30–1000 nm in size. These steps occurred at intersections of dislocation walls or GNBs and grain boundaries.

The dislocation structure in two grains separated by a $43.8^{\circ}2910$ grain boundary in hydrogen-charged Ni is shown in Fig. 9b. The microstructure consisted of a dislocation cell structure, with a high density of GNBs, particularly in the left grain. Overall, the microstructure appeared more organized than in the uncharged alloy, with the dislocation walls straight and densely packed. The grain boundaries were intact and straight with no observable nano- or microvoids, and showed no significant steps even at intersections with GNBs.

To gain further understanding of the state of deformation, ASTAR orientation mapping was used to generate reference orientation deviation (ROD) maps from regions in adjacent grains as a function of distance from the grain boundary. Mapping the orientation deviation of each point in a grain with respect to a reference point immediately adjacent to the grain boundary allowed for comparison of orientation gradients in neighboring grains with the grain boundary misorientation removed. In uncharged Ni, the RODs that developed near the grain boundary in both neighboring grains were generally of similar magnitude and distribution. Larger orientation deviations occurred several micrometers from the grain boundary, frequently across GNBs. An example of these observations is presented in Fig. 9c. The ROD maps are overlaid on the images of the dislocation structures and colored according to the magnitude of the ROD; the reference point for each grain is indicated by a black dot with a white border. No significant difference in the magnitude of the ROD occurred on either side of the grain boundary. That is, the strain is communicated across the grain boundary. Parallel to and within approximately 4 µm of the grain boundary, the largest ROD in either grain was approximately 1-2°. Regions in the interior of the grain exhibited RODs of less than 7°.

In hydrogen-charged Ni, the RODs, especially in the vicinity of the grain boundary, tended to be larger than in uncharged Ni. Significant differences occurred in the magnitude of the RODs that developed over similar distances from the grain boundary in the adjacent grains, such that the RODs tended to be greater in one grain than in the other. These

differences can be seen in Fig. 9d, which shows the magnitude of the RODs near and parallel to the grain boundary reaching up to approximately 8° and 2-3° in grains I and II, respectively. Across the interior of grain I, the magnitude of the orientation deviation reached approximately 12° with respect to the reference point in grain I, while in grain II, the magnitude stayed at approximately 2–3° across the grain interior. This result indicates that the deformation state may have been more evolved in grain I than in grain II and that hydrogen restricted the communication of strain across the grain boundary. Both the evolved microstructural state and the larger RODs are consistent with hydrogen enhancing the plasticity.

To further explore the impact of the deformed microstructure, the dislocation structure was compared for matching intergranular facets. Beneath the matching facets, the deformation microstructure generated at a failure strain of approximately 15% consisted of a dislocation cell structure on which dense, elongated dislocation walls and microbands were superimposed. An example of the microstructure in the adjoining grains is shown in Fig. 10. Fractographs from the mating surfaces are presented in Fig. 10a and b, and the bright-field STEM images in Fig. 10c. As can be seen from Fig. 10c, both fracture surfaces were not straight, but contained step-like features, which correlate to the steps on the fracture surfaces. The evolved microstructural state was qualitatively similar in both grains, consisting of dense dislocation walls, dislocation cells, GNBs, and microbands. However, regions exist in both grains that appear to contain more deformation bands than other regions, suggesting local differences in evolution of the deformed state.

A more significant difference between the two grains was observed in the ROD maps. The ROD maps are shown superimposed on STEM images of the underlying structures in Fig. 11, with the reference points on the fracture surfaces indicated by the black dots with white borders. The locations from which the ROD maps were acquired are indicated by the boxed regions in Fig. 10c. In comparing the two grains, it is evident that the RODs that developed within approximately 10 μm of the fracture surface were larger in the left grain (12–13°), Fig. 11a, than in the right grain (6–7°), Fig. 11b. This result is consistent with that observed across the internal grain boundaries, an example of which was shown in Fig. 9d. That is, the ROD distribution is non-uniform in adjacent grains, which is in marked contrast to that observed across grain boundaries in uncharged Ni.

4. Discussion

The need for hydrogen to be accumulated on the grain boundary to cause intergranular failure is without question, as removal of hydrogen from the metal during the tensile test results in a return to a transgranular failure mode [4]. However, neither the hydrogen coverage dependence on the boundary orientation nor the concentration of hydrogen needed on a particular grain boundary to cause it to fail by decohesion are known. It has been suggested that twin boundaries are important for promoting hydrogen-induced intergranular failure [35]. However, this result is not consistent with the improved hydrogen tolerance achieved through grain boundary engineering, which introduces a high fraction of twin boundaries [23]. Furthermore, Tehranchi and Curtin reported no absorption of hydrogen on twin boundaries [25]. Wang et al., used a grand canonical thermodynamic model of molecular dynamics simulations to determine the hydrogen-induced reduction of the ideal separation energy, and concluded it would be challenging to achieve the concentration required for failure by pure decohesion under conventional and practical hydrogen-charging conditions in Fe [20] and Ni [36]. The latter conclusion is similar to that reached by Tehranchi and Curtin who concluded that the equilibrium hydrogen concentration on a grain boundary was insufficient to cause intergranular failure and that during the deformation either diffusion of hydrogen through the lattice and along the grain boundary or dynamic crack growth was necessary [25]. These latter results support the need for additional driving forces to cause hydrogen-induced intergranular

failure.

However, the need for additional factors has been challenged recently as Ni containing 4660 at ppm of hydrogen that was subjected to slow strain rate uniaxial mechanical testing at 77 K failed intergranularly [24]. Harris et al. argued that at 77 K, hydrogen will not be transported with mobile dislocations, meaning it should serve as a solid solution strengthener, and that the hydrogen concentration needed to cause intergranular failure was achieved by diffusion through the lattice and along grain boundaries prior to the mechanical test [24]. These results are consistent with those reported by Lassila and Birnbaum in the late 1980s [15,16]. Both studies assumed that the deformation prior to cracking played no role in the intergranular failure. However, neither study considered that hydrogen on the grain boundary can increase the emission of dislocations from grain boundary sources [37] and could limit stress-driven grain growth [38].

Harris et al. dismissed the role of a microstructure related stress in the hydrogen-induced intergranular failure at 77K and RT as the flow stress, work hardening rates and the dislocation structures were similar at a true strain of 0.1 in uncharged and hydrogen-charged Ni [24]. The lack of a difference in the dislocation structures generated in absence and presence of hydrogen is in marked contrast to the results of other recent studies [18,19,21,39-41]. The observations by Wang et al. are particularly relevant, as the comparison of dislocation structures was made following torsional processing, which allows the deformed microstructure to be assessed at the same plastic strain [41]. They reported the dislocation cell size was smaller and the cell walls thicker in hydrogen-charged than in uncharged Ni. Further evidence for hydrogen impacting the evolution of the dislocation structure is the observation of second-generation microbands at 9.5% strain, see Fig. 7; these bands do not typically form in uncharged Ni until strains of over 50% [34]. Although Harris et al. do not consider microstructure related stresses important, they attributed the decrease in the true fracture strain at room temperature to hydrogen transport by dislocations to grain boundaries increasing the hydrogen concentration on grain boundaries [24]. This hydrogen transport mechanism is an element of the hydrogen-enhanced plasticity explanation of hydrogen-induced intergranular failure [18,19,21,22,30]. However, it is likely effective only at low strains where strain transfer across a grain boundary is dislocation-

Based on the experimental observations reported herein, it will be argued that hydrogen-enhanced plasticity establishes the local conditions that ultimately promote intergranular failure by decohesion. To recap, the main findings of this study were that hydrogen:

- 1. reduced the development of a < 111 > texture parallel to the loading axis, reduced the average rotations of individual grains parallel to the loading axis, and reduced the deformation-induced elongation of grains; and
- Induced larger out-of-surface displacements and larger localized orientation deviations within individual grains, caused larger RODs to develop on one side of grain boundaries than the other in both intact and ruptured grain boundaries, and accelerated evolution of more organized dislocation structures.

These two groupings appear contradictory as the first group supports hydrogen reducing the plasticity and the second supports hydrogen increasing the plasticity. One common mechanism must exist to reconcile the observations in both groups. As texture development, grain rotation, and grain elongation require dislocation slip to occur on specific systems [2,3], these group 1 observations must correlate with the behavior of dislocations and be dependent on the evolved dislocation structures at the microscale.

In the absence of hydrogen at the dislocation level within a single grain, the microstructure evolves from dislocation-dislocation interactions to formation of dislocation tangles, and then to dislocation cell formation [43,44]. As strain increases, the cell size decreases, the

dislocation density in cell walls increases, and larger rotations develop between cells, which can evolve into the formation of a sub-grain structure [34,43,45]. GNBs may form either concurrently with or after dislocation cell formation [1,46-48]. Essentially, GNBs separate regions in which the magnitude of the deformation is locally different, or the amount of slip on activated slip systems varies. If a GNB forms within a grain, then the angular misorientation across the GNB wall increases with increasing strain, leading to further microstructural refinement [49]. The dislocation cell structure modifications generally occur within regions separated by GNBs. The specific dislocation structures that are formed will be dependent on the initial orientation of the grain with respect to the loading direction as well as the local influence of neighboring grains and grain boundaries [1-3,47,49]. Less is known about how hydrogen influences these changes in microstructure with increasing strain. However, from knowledge of the effects of hydrogen on discrete dislocations, i.e., enhanced dislocation generation, higher dislocation mobility, restricted cross-slip, and smaller equilibrium separation distance between dislocations [50], it would be predicted that hydrogen would: accelerate development of a dislocation cell structure [41]; reduce the minimum cell size, since it is proportional to dislocation interspacing in the wall [51]; and increase the density of dislocations in the cell walls by enabling tighter packing of dislocations within the cell walls. These hydrogen effects provide a consistent explanation of the differences in the observed microstructures seen in Figs. 5-11.

The accumulation of hydrogen in the dislocation structures will influence how they interact with and emit new dislocations. Assuming dislocations emitted from a cell wall transport hydrogen, cross-slip of dislocations will be restricted as they move across the cell interior [52]. These restrictions will influence the local development of orientation deviations within a single grain, constraining and decoupling localized regions and thus allowing rotations in opposing directions to develop. Consequently, large-scale rotation of the grains on average will be hindered, see Figs. 2 and 4. This inhibiting of grain rotation has been found to modify the motion of the grain boundary [53]. Furthermore, for the same reasons hydrogen inhibits cross-slip [52], it is suggested that it can effectively lock the cell structure in position, as large-scale reorganization would require a redistribution of hydrogen and an increase in the total dislocation line energy. Consequently, large-scale, average grain rotations (Figs. 2 and 4) and elongation of the grains in the loading direction (Fig. 3) will be restricted by hydrogen and its influence on dislocation structures. Thus, the seemingly disparate results listed in groups 1 and 2 are reconciled through the effects of hydrogen on the plasticity and the generation of the resulting microstructure.

The observation that the out-of-surface distortion was greater in the presence of hydrogen (compare Fig. 1b and c) is consistent with prior studies on slip steps and surface distortions [21,22,54–56]. Both observations of slip step height increases and density differences due to hydrogen are consistent with increased plasticity. Although such results are often taken as evidence for increased slip planarity, it is important to remember that the slip steps on the surface reflect only specific slip system intersections with the surface and do not represent the totality of the plasticity; see Fig. 10 and references [57,58]. Bilotta et al. reported that on cyclic loading of a martensitic steel, the displacement out of the crack plane was greater in the presence than the absence of hydrogen [56]. This observation was interpreted as hydrogen enhancing the plasticity in the vicinity of the crack but not decreasing the size of the plastic zone.

Strain transfer across grain boundaries at low strains is dislocation-mediated and involves the accommodation of dislocations into, and the emission of new dislocations from, the grain boundary [42]. The residual dislocation generated in the grain boundary by this transmission process has a Burgers vector equal to the difference in the Burgers vector of the accommodated and emitted dislocations, and it can create local rotations, steps and disorder in the grain boundary. The increased disorder would increase the density of low energy trap sites for

hydrogen. It is not known if the presence of hydrogen in the grain boundary alters this strain transmission process. Ignoring the changes in hydrogen accommodation associated with the disruption of the grain boundary structure and orientation, failure along the grain boundary would naturally follow the steps, leaving steps on the fracture surface. The micrographs presented in Fig. 9b shows no steps on the intact grain boundary whereas Fig. 10c shows steps in the failed grain boundary. Further work on strain transfer across grain boundaries in the presence of hydrogen is needed to ascertain if the formation of these steps is an important feature in the selection of the grain boundaries along which fracture will occur.

Maintaining compatibility across grain boundaries requires that the adjoining grains deform cooperatively, such that the displacement on each side of the boundary is equivalent [5]. The ROD maps, Fig. 9d and 11, show the development of higher orientation deviations in one grain than the adjoining one in the presence of hydrogen. This observation suggests that the strain developed in one grain was not accommodated equivalently in the other grain, i.e., the mechanism of strain communication across the grain boundary was hindered by the locked evolved microstructural states. A reduced ability of grains to cooperatively deform in response to the applied load would thus enhance the local influence of the grain boundary on the deformation in adjacent regions, and subsequently would also tend to exacerbate differences in the response of adjacent grains to boundary-induced constraints. Additionally, such effects could impact the mobility of the grain boundary [53]. This development of a compatibility constraint across the grain boundary in response to the applied load and the microstructure-generated local stress and the locking of the microstructure in a specific configuration by hydrogen makes the grain boundary the weakest link in the system. Consequently, the system response to further increases in the applied load will be to fail along the grain boundary. This mechanism explains the observation of the microcracks seen in Fig. 1, as the deformation is enhanced along the gauge length, these factors can occur locally throughout the gauge length. The propagation of the intergranular crack will require these conditions are satisfied on either side of contiguous grain boundaries. If this condition is not satisfied, the intergranular crack propagation will be halted.

In considering the results of Lassila and Birnbaum [15,16] and Harris et al. [24] at low temperature, the following posit is proposed. At low temperatures, the higher strain to failure will correlate with a more evolved dislocation structure. The microstructure formed in the presence of hydrogen may be modified by hydrogen-accelerated emission of dislocations from grain boundary sources [37]. This microstructure in conjunction with the latent hardening from the interstitial hydrogen in the grain interior would increase the local stress. Furthermore, the presence of hydrogen on the grain boundary may inhibit grain boundary mobility and rotation. With increasing strain, the grain boundary would eventually fail as the matrix is unable to support the applied load by dislocation slip or other deformation mechanisms.

5. Conclusions

A complete understanding of the deformation response across multiple spatial scales allows for an explanation of hydrogen-induced intergranular failure by decohesion that simultaneously accounts for the observed plasticity. Without the additional constraints imposed by the local microstructural state the level of hydrogen on the grain boundary has been indicated to be insufficient to cause failure by hydrogen-induced decreases in the cohesive strength. Thus, it is a combination of the additional constraints imposed by the influence of hydrogen on deformation as well as the reduction in grain boundary cohesive energy that induces intergranular failure.

It is also concluded that assessing the dislocation structures from either surface damage observations or macroscopic stress-strain data is challenging as the interpretation is based on assumed behavior of dislocations and the self-organization of dislocation structures at high

strains. As the influence of hydrogen on the self-organization of dislocations in the nascent phase, it is necessary to observe the dislocation structures.

Acknowledgements

KMB, SW and IMR gratefully acknowledge the support of the National Science Foundation [NSF CMMI-1406462]. KMB acknowledges support from the National Science Foundation Graduate Research Fellowship Program [NSF 2013148159]. AN acknowledges support from JFE Steel Corporation, KMB acknowledges partial financial support from the International Institute for Carbon-Neutral Energy Research (WPI-I2CNER) of Kvushu University sponsored by the World Premier International Research Center Initiative (WPI), MEXT, Japan. The authors gratefully acknowledge Dr. Alberto Mello and Professor Michael Sangid of Purdue University for their collaboration in performing the in situ SEM straining experiment. Professor Petros Sofronis (University of Illinois at Urbana-Champaign) and Dr. Kelly Nygren (Cornell University) are thanked for their comments on this work. The electron microscopy was carried out using facilities and instrumentation in the Center for Microanalysis of Materials at the University of Wisconsin-Madison, which is partially supported by the NSF Materials Research Science and Engineering Center [NSF DMR-1720415].

Appendix A. Supplementary data

Supplementary data to this article can be found online at https://doi.org/10.1016/j.msea.2019.05.036.

Data availability

The raw data required to reproduce these findings are available to download from https://data.mendeley.com/datasets/j9vpbp6nrm/. The processed data required to reproduce these findings are available to download from https://data.mendeley.com/datasets/j9vpbp6nrm/ [59].

References

- N. Hansen, X. Huang, G. Winther, Effect of grain boundaries and grain orientation on structure and properties, Metall. Mater. Trans. A 42 (3) (2011) 613–625.
- [2] G. Winther, Slip systems extracted from lattice rotations and dislocation structures, Acta Mater. 56 (9) (2008) 1919–1932.
- [3] G. Winther, Slip systems, lattice rotations and dislocation boundaries, Mater. Sci. Eng. A 483–484 (2008) 40–46.
- [4] T. Boniszewski, G.C. Smith, The influence of hydrogen on the plastic deformation ductility, and fracture of nickel in tension, Acta Metall. 11 (3) (1963) 165–178.
- [5] J.P. Hirth, The influence of grain boundaries on mechanical properties, Metall. Trans A 3 (12) (1972) 3047–3067.
- [6] R.M. Latanision, H. Opperhauser, Intergranular embrittlement of nickel by hydrogen effect of grain-boundary segregation, Metall. Trans A 5 (2) (1974) 483–492.
- [7] K. Yoshino, J. McMahon C.J., The cooperative relation between temper embrittlement and hydrogen embrittlement in a high strength steel, Metall. Trans. 5 (2) (1974) 363–370.
- [8] R.A. Oriani, P.H. Josephic, Equilibrium and kinetic studies of the hydrogen-assisted cracking of steel, Acta Metall. 25 (9) (1977) 979–988.
- [9] S.M. Bruemmer, R.H. Jones, M.T. Thomas, D.R. Baer, Fracture mode transition of iron in hydrogen as a function of grain boundary sulfur, Scripta Metall. 14 (1) (1980) 137–141.
- [10] T.S.F. Lee, R.M. Latanision, Hydrogen induced intergranular cracking of nickel and nickel-base alloys, J. Met. 32 (8) (1980) 40 40.
- [11] R.P. Messmer, C.L. Briant, The role of chemical bonding in grain boundary embrittlement, Acta Metall. 30 (2) (1982) 457–467.
- [12] R.H. Jones, S.M. Bruemmer, M.T. Thomas, D.R. Baer, Hydrogen pressure dependence of the fracture mode transition in nickel, Metall. Trans. A (8) (1983) 1729–1736.
- [13] J. Kameda, C.J. McMahon Jr., Solute segregation and hydrogen-induced intergranular fracture in an alloy steel, Metall. Trans. A 14A (5) (1983) 903–911.
- [14] K.S. Shin, M. Meshii, Effect of sulfur segregation and hydrogen charging on intergranular fracture of iron. Acta Metall. 31 (10) (1983) 1559–1566.
- [15] D.H. Lassila, H.K. Birnbaum, Intergranular fracture of nickel: the effect of hydrogensulphur co-segregation, Acta Metall. 35 (7) (1987) 1815–1822.
- [16] D.H. Lassila, H.K. Birnbaum, The effect of diffusive segregation on the fracture of

- hydrogen charged nickel, Acta Metall. 36 (10) (1988) 2821-2825.
- [17] C.J. McMahon Jr., Hydrogen-induced intergranular fracture of steels, Engin, Frac. Mech. 68 (6) (2001) 773–788.
- [18] M.L. Martin, B.P. Somerday, R.O. Ritchie, P. Sofronis, I.M. Robertson, Hydrogeninduced intergranular failure in nickel revisited, Acta Mater. 60 (6–7) (2012) 2739–2745.
- [19] S. Wang, M.L. Martin, P. Sofronis, S. Ohnuki, N. Hashimoto, I.M. Robertson, Hydrogen-induced intergranular failure of iron, Acta Mater. 69 (2014) 275–282.
- [20] S. Wang, M.L. Martin, I.M. Robertson, P. Sofronis, Effect of hydrogen environment on the separation of Fe grain boundaries, Acta Mater. 107 (2016) 279–288.
- [21] K.E. Nygren, K.M. Bertsch, S. Wang, H. Bei, A. Nagao, I.M. Robertson, Hydrogen embrittlement in compositionally complex FeNiCoCrMn FCC solid solution alloy, Curr. Opin. Solid State Mater. Sci. 22 (1) (2018) 1–7.
- [22] K.E. Nygren, S. Wang, K.M. Bertsch, H. Bei, A. Nagao, I.M. Robertson, Hydrogen embrittlement of the equi-molar FeNiCoCr alloy, Acta Mater. 157 (2018) 218–227.
- [23] S. Bechtle, M. Kumar, B.P. Somerday, M.E. Launey, R.O. Ritchie, Grain-boundary engineering markedly reduces susceptibility to intergranular hydrogen embrittlement in metallic materials, Acta Mater. 57 (14) (2009) 4148–4157.
- [24] Z.D. Harris, S.K. Lawrence, D.L. Medlin, G. Guetard, J.T. Burns, B.P. Somerday, Elucidating the contribution of mobile hydrogen-deformation interactions to hydrogen-induced intergranular cracking in polycrystalline nickel, Acta Mater. 158 (2018) 180–192
- [25] A. Tehranchi, W.A. Curtin, Atomistic study of hydrogen embrittlement of grain boundaries in nickel: I. Fracture, J. Mech. and Phys. of Sols 101 (2017) 150–165.
- [26] G.L. Krasko, G.B. Olson, Effect of hydrogen on the electronic structure of a grain boundary in iron, Solid State Commun. 79 (2) (1991) 113–117.
- [27] L. Zhong, R. Wu, A. Freeman, G. Olson, Charge transfer mechanism of hydrogeninduced intergranular embrittlement of iron, Phys. Rev. B 62 (21) (2000) 13938–13941.
- [28] W.T. Geng, A.J. Freeman, G.B. Olson, Y. Tateyama, T. Ohno, Hydrogen-promoted grain boundary embrittlement and vacancy activity in metals: insights from ab initio total energy calculations, Mater. Trans. 46 (4) (2005) 756–760.
- [29] D.E. Jiang, E.A. Carter, First principles assessment of ideal fracture energies of materials with mobile impurities: implications for hydrogen embrittlement of metals, Acta Mater. 52 (16) (2004) 4801–4807.
- [30] I.M. Robertson, P. Sofronis, A. Nagao, M.L. Martin, S. Wang, D.W. Gross, K.E. Nygren, Hydrogen embrittlement understood, Metall. Mater. Trans. A 46 (2015) 1–19.
- [31] A.D. Darbal, M. Gemmi, J. Portillo, E. Rauch, S. Nicolopoulos, Nanoscale Automated phase and orientation mapping in the TEM, Microscopy Today 20 (06) (2012) 38–42.
- [32] F. Bachmann, R. Hielscher, H. Schaeben, Grain detection from 2d and 3d EBSD data—specification of the MTEX algorithm, Ultramicroscopy 111 (12) (2011) 1720–1733.
- [33] A. Kimura, H.K. Birnbaum, Effects of H on flow stress of Ni, Acta Metall. 35 (5) (1987) 1077–1088.
- [34] D.A. Hughes, N. Hansen, Microstructural evolution in nickel during rolling and torsion. Mater. Sci. Technol. 7 (6) (1991) 544–553.
- [35] M. Seita, J.P. Hanson, S. Gradečak, M.J. Demkowicz, The dual role of coherent twin boundaries in hydrogen embrittlement. Nat. Commun. 6 (2015) 6164.
- [36] S. Wang, private communication, (2018).
- [37] B. Kuhr, D. Farkas, I.M. Robertson, Atomistic studies of hydrogen effects on grain boundary structure and deformation response in FCC Ni, Comput. Mater. Sci. 122 (2016) 92–101.
- [38] D.S. Gianola, D. Farkas, M. Gamarra, M.-R. He, The role of confinement on stress-

- driven grain boundary motion in nanocrystalline aluminum thin films, J. Appl. Phys. 112 (12) (2012) 124313.
- [39] K.M. Bertsch, K.E. Nygren, S. Wang, H. Bei, A. Nagao, The Role of the Dislocation Microstructure and Grain Interactions in Hydrogen Embrittlement of the High-Entropy Alloy FeNiCoCrMn, Personal Communication, 2018.
- [40] Y.Z. Chen, H.P. Barth, M. Deutges, C. Borchers, F. Liu, R. Kirchheim, Increase in dislocation density in cold-deformed Pd using H as a temporary alloying addition, Scripta Mater. 68 (9) (2013) 743–746.
- [41] S. Wang, A. Nagao, K. Edalati, Z. Horita, I.M. Robertson, Influence of hydrogen on dislocation self-organization in Ni, Acta Mater. 135 (2017) 96–102.
- [42] J. Kacher, B. Eftink, B. Cui, I.M. Robertson, Dislocation interactions with grain boundary, Curr. Opin. Solid State Mater. Sci. 18 (2014) 227–243.
- [43] U.F. Kocks, H. Mecking, Physics and phenomenology of strain hardening: the FCC case, Prog. Mater. Sci. 48 (3) (2003) 171–273.
- [44] M. Sauzay, L.P. Kubin, Scaling laws for dislocation microstructures in monotonic and cyclic deformation of fcc metals, Prog. Mater. Sci. 56 (6) (2011) 725–784.
- [45] D. Kuhlmann-Wilsdorf, N. Hansen, Geometrically necessary, incidental and subgrain boundaries, Scripta Metall. Mater. 25 (7) (1991) 1557–1562.
- [46] X. Huang, G. Winther, Dislocation structures. Part I. Grain orientation dependence, Phil. Mag. 87 (33) (2007) 5189–5214.
- [47] N. Hansen, Plastic behavior of metals: large strains, in: K.H.J. Buschow, R.W. Cahn, M.C. Flemings, B. Ilschner, E.J. Kramer, S. Mahajan, P. Veyssière (Eds.), Encyclopedia of Materials: Science and Technology, second ed., Elsevier, Oxford, 2001, pp. 7040–7050.
- [48] D.A. Hughes, N. Hansen, High angle boundaries formed by grain subdivision mechanisms, Acta Mater. 45 (9) (1997) 3871–3886.
- [49] N. Hansen, R.F. Mehl, A. Medalist, New discoveries in deformed metals, Metall. Mater. Trans. A 32 (12) (2001) 2917–2935.
- [50] I.M. Robertson, The effect of hydrogen on dislocation dynamics, Eng. Fract. Mech. 68 (6) (2001) 671–692.
- [51] D.L. Holt, Dislocation cell formation in metals, J. Appl. Phys. 41 (8) (1970) 3197–3201.
- [52] P.J. Ferreira, I.M. Robertson, H.K. Birnbaum, Hydrogen effects on the character of dislocations in high-purity aluminum, Acta Mater. 47 (10) (1999) 2991–2998.
- [53] Z.T. Trautt, Y. Mishin, Grain boundary migration and grain rotation studied by molecular dynamics, Acta Mater. 60 (5) (2012) 2407–2424.
- [54] M. Ménard, J.M. Olive, A.M. Brass, I. Aubert, Effects of hydrogen charging on surface slip band morphology of a type 316L stainless steel, in: S.A. Shipilov, R.H. Jones, J.M. Olive, R.B. Rebak (Eds.), Environment-Induced Cracking of Materials, Elsevier, Amsterdam, 2008, pp. 179–188.
- [55] K.A. Nibur, D.F. Bahr, B.P. Somerday, Hydrogen effects on dislocation activity in austenitic stainless steel. Acta Mater. 54 (10) (2006) 2677–2684.
- [56] G. Bilotta, G. Henaff, D. Halm, M. Arzaghi, Experimental measurement of out-ofplane displacement in crack propagation under gaseous hydrogen, Int. J. Hydrogen Energy 42 (15) (2017) 10568–10578.
- [57] D.W. Gross, K. Nygren, G.J. Pataky, J. Kacher, H. Sehitoglu, I.M. Robertson, The evolved microstructure ahead of an arrested fatigue crack in Haynes 230, Acta Mater. 61 (15) (2013) 5768–5778.
- [58] S. Wang, K.E. Nygren, A. Nagao, P. Sofronis, I.M. Robertson, On the failure of surface damage to assess the hydrogen-enhanced deformation ahead of crack tip in a cyclically loaded austenitic stainless steel, Scripta Mater (166) (2019) 102–106.
- [59] K.M. Bertsch, S. Wang, A. Nagao, I. Robertson, Hydrogen-induced Compatibility Constraints across Grain Boundaries Drive Intergranular Failure of Ni vol. 1, Mendeley Data, 2018, https://data.mendeley.com/datasets/gjrstsg253/draft?a=6d1964fc-b877-47bd-8b35-bef031832098.